The Astrophysical Journal, in press. 28mar2000

A Multi-Transition HCO^+ Study in NGC 2264G: Anomalous Emission of the J=1→0 line

José M. Girart[1], Robert Estalella[2], Paul T. P. Ho[3], and Alexander L. Rudolph[4,5],

ABSTRACT

We present multi-transition observations of the HCO^+ molecule toward the very young star forming region associated with the NGC 2264G molecular outflow. Anomalous emission is observed in the lowest rotational transition: the J=4→3 and J=3→2 transitions clearly trace the dense core encompassing the exciting source of the molecular outflow, whereas the HCO^+ J=1→0 is barely detected at a much lower intensity and has a much broader line shape. Analysis of the data strongly suggests that the HCO^+ J=1→0 emission arising from the core is being absorbed efficiently by a cold low density envelope around the core or a foreground cloud. This result seems exceptional, yet the J=1→0 HCO^+ and HCN emission from other dense cores (especially those in giant molecular clouds) may be affected. In these cases, the rare isotopes of these molecules and higher rotational transitions of the main isotopes should be used to study these regions. Two quiescent clumps, JMG99 G1 and G2, are detected in the blue lobe of the NGC 2264G molecular outflow, close to shock excited near-IR H_2 knots. These clumps belong to the class of radiatively excited clumps, i.e., the radiation from the shock evaporates the dust mantles and initiates a photochemical process, enhancing the emission of the HCO^+.

Subject headings: ISM: individual: NGC 2264G— ISM: jets and outflows — ISM: molecules — radio lines: ISM — stars: formation

1. Introduction

The NGC 2264G molecular outflow was first discovered in a survey of molecular gas toward the NGC 2264 giant cloud complex (Margulis & Lada 1986). Margulis, Lada & Snell (1988) found that this molecular outflow has a high degree of collimation and a large mechanical luminosity. Detailed observational studies have revealed several interesting characteristics (Lada & Fich 1996): 1) the collimation of the outflowing gas increases with the flow velocity and the distance to the source, 2) the velocity distribution is well described by a single "Hubble" law (i.e., a linear velocity increase with distance from the powering source) and, 3) the flow mass distribution follows a power-law with respect to the velocity, as has been

[1]Department of Astronomy, University of Illinois, 1002 W. Green Street, Urbana, IL 61801, USA

[2]Departament d'Astronomia i Meteorologia, Universitat de Barcelona, Av. Diagonal 647, E-08028 Barcelona, Spain

[3]Harvard-Smithsonian Center for Astrophysics, 60 Garden Street, Cambridge, MA 02138, USA

[4]Department of Physics, Harvey Mudd College, Claremont, CA 91711, USA

[5]NSF CAREER Fellow

observed in other well collimated molecular outflows. Several H_2 knots arise within the molecular outflow, although there are remarkable differences in the morphology between the H_2 associated with the red lobe and that associated with the blue lobe (Davis & Eislöffel 1995). These authors suggest that this may be due to different H_2 excitation mechanisms. On the other hand, Fich & Lada (1997) found that material with the highest CO flow velocities, which have a jet-like morphology, appear to emerge deflected from H_2 knots. Both the deflection of the material with the highest CO flow velocities and the H_2 knots may be consequence of a temporal change in the direction of the outflow axis.

Close to the geometrical center of the molecular outflow there are several near infrared sources (Margulis et al. 1990) and IRAS 06384+0958. Curiel & Rodríguez (1989) found a radio continuum source, VLA 1, located within the error ellipse of the IRAS source and that laid close to the near infrared source IRS 1. They proposed that these three sources trace the same object, the driving source of the molecular outflow. However, ammonia and deep continuum VLA observations identified a likelier candidate for the powering source of the molecular outflow, VLA 2, a deeply embedded low mass star surrounded by a core of $\sim 6\ M_\odot$ (Gómez et al. 1994). Further submillimeter continuum observations confirmed these results (Ward-Thompson, Eiroa, & Casali 1995), and identified this source as a Class 0 protostar with a bolometric luminosity of $\sim 12\ L_\odot$. The mechanical luminosity from the ionized wind traced by the radio continuum emission is of the same order as the mechanical luminosity of the molecular outflow and comparable to the stellar luminosity, implying that the driving mechanism of the flow is extraordinarily efficient (Gómez et al. 1994; Lada & Fich 1996).

Observations of HCO^+, a high density tracer, have shown that it can be a useful and complementary tracer to study molecular outflows and their interaction with the dense ambient medium (e. g., Girart et al. 1999). HCO^+ has also been used to study the properties of the dense cores where stars are being formed (e. g., Hogerheijde et al. 1997). In interpreting these observations it is necessary to be aware of the role that self-absorption can play in shaping HCO^+ line profiles (as well as profiles of other high-density tracers). In the typical molecular cloud core, strong, narrow self-absorption is often seen in the HCO^+ J=1→0 (e. g., Langer et al. 1978; Hogerheijde et al. 1997), although it can also be seen in higher transitions in massive dense cores (e. g., Heaton et al. 1993; van Dishoeck et al. 1995). The narrow velocity range of this self-absorption is caused by the low velocity dispersion of these cool, overlying layers. In this paper we present a multi-transition HCO^+ study from observations carried out toward the NGC 2264G molecular outflow. The HCO^+ J=1→0 emission from NGC 2264G is unusual because instead of showing the narrow self-absorption feature, it shows evidence of complete absorption, by a cold, low-density foreground cloud, of the HCO^+ J=1→0 line emission from the core surrounding the driving source of the NGC 2264G outflow, obscuring all velocities out to the outflow velocities (see § 4.2 and 5.1.1), while the higher HCO^+ transitions are unaffected by this low density cloud.

2. Observations

2.1. FCRAO

The HCO^+ J=1→0 (89.1885 GHz) emission was mapped with the 14-m FCRAO[6] telescope using the QUARRY 15-element receiver array in 1994 April and 1995 December. At the observing frequency the main-beam efficiency is $\eta_{\rm MB} \sim 50\%$ and the angular resolution is $\sim 58''$. We used the FAAS autocorrela-

[6]The Five College Radio Astronomy Observatory is supported by the National Science Foundation and the Commonwealth of Massachusetts and is operated by permission of the Metropolitan District Commission.

tion spectrometer with an effective bandwidth of 40 MHz and a velocity resolution of 0.26 km s^{-1}. The observations were performed in the total power mode. Typical system temperatures of 400–650 K were obtained during the observations. Using Nyquist-sampled (25″ spacings) footprints we mapped a total area of $\sim 11' \times 5'$ with a PA= 90°, covering the molecular outflow. The averaged T_A^* rms noise achieved was $\sim$ 0.1 K for a velocity resolution of 0.26 km s^{-1}. The line intensities are given in main-beam brightness temperature, $T_{\rm MB} = T_A^*/\eta_{\rm MB}$.

2.2. Haystack

Several HCO^+ J=1→0 spectra toward the NGC 2264G core were taken with the 37 m telescope of the Haystack Observatory[7] in 1995 December and 1996 February and March. At the frequency of this transition the main-beam efficiency is $\sim$ 18% and the angular resolution is $\sim$ 25″. We used a cooled SIS dual-channel receiver and a 4096-lag autocorrelation spectrometer with a bandwidth of 53.3 MHz. The observations were performed in frequency-switching mode. After Hanning smoothing, the velocity resolution was $\sim$ 0.2 km s^{-1}. Vane calibration was used to calibrate the spectra. The spectra were corrected for elevation-dependent gain variations and for atmospheric attenuation. The system temperatures measured during the observations were $\sim$ 250 K. The typical T_A^* rms noise achieved was $\sim$ 0.1 K for the fore-mentioned velocity resolution.

2.3. JCMT

HCO^+ J=4→3 (356.7343 GHz) and $H^{13}CO^+$ J=4→3 (346.9985 GHz) observations were carried out with the 15-m James Clerk Maxwell Telescope[8] (JCMT) in 1996 February. We used the B3i receiver and the 2048 channel DAS spectrometer that provided an effective spectral bandwidth and resolution of 100 and 0.068 km s^{-1} respectively. The main-beam efficiency and the angular resolution at 356 GHz were $\sim$ 58% and $\sim$ 13.″5 respectively. System temperatures ranged 600–1000 K. We used the raster map technique to map a region of about 140″ × 42″ covering the energy source of the molecular outflow and part of the blue lobe of the molecular outflow, where the near-IR H_2 is detected. We also took several HCO^+ J=4→3 spectra at different positions within the red lobe. These spectra and the $H^{13}CO^+$ J=4→3 observations were made in the position switching mode. Data reduction were performed using the SPECX software package.

2.4. OVRO

The HCO^+ J=1→0 line was also mapped with the millimeter-wave array at Owens Valley Radio Observatory[9] (OVRO). The observations were carried out in its low and equatorial configurations during 1996 October, 1997 March and May. The digital correlator was configured in order to observe simultaneously

[7]Radio Astronomy at Haystack Observatory of the Northeast Radio Observatory Corporation was supported by the National Science Foundation.

[8]The James Clerk Maxwell Telescope is operated by the Royal Observatories on behalf of the Particle Physics and Astronomy Research Council of the United Kingdom, the Netherlands Organisation for Scientific Research and the National Research Council of Canada.

[9]The Owens Valley millimeter-wave array is supported by NSF grant AST 96-13717 and by the Norris Planetary Origins Project.

the HCO^+ J=1→0 line in the upper sideband and the SiO J=2→1 line (86.8470 GHz) in the lower sideband. For each of these two lines we used two 64 channel windows of 32 and 8 MHz bandwidth, providing 1.73 and 0.43 km s^{-1} velocity resolution, respectively. In addition, a 1 GHz window was used for continuum observations in each sideband. We made a two point mosaic, covering the core and the blue lobe where near-IR H_2 is detected. One field was centered at the position of the powering source of the molecular outflow ($\alpha(J2000) = 06^h41^m10\overset{s}{.}72$ and $\delta(J2000) = 09°55'58\overset{''}{.}9$), and the other was located 48″ west of this position. The phase calibrator used was 0528+134, and the passband calibrators were 3C273 and 3C454.4. System temperatures typically ranged 300–1100 K during the observations. The data were calibrated using the MMA software, developed at Caltech. Maps were made using natural weighting which yielded a synthesized beam of $5\overset{''}{.}3 \times 4\overset{''}{.}7$, PA= $-46°$.

2.5. CSO

Observations of the HCO^+ J=3→2 (267.5576 GHz) line were carried out with the Caltech Submillimeter Observatory[10] (CSO) 10.4 m telescope in 1997 March and April. The 230 GHz receiver was used in conjunction with 50 MHz and 500 MHz acousto-optical spectrometers, which provided velocity coverages of 56 and 560 km s^{-1} at 267 GHz. Since the antenna was covered with a tent during the observations, the pointing and calibration were checked every few hours using Mars (we note that the tent was almost transparent at the frequencies observed resulting in only a small decrease in the antenna efficiency). At the measured frequency the beam size was ∼ 26″, and the main-beam efficiency was ∼51%. System temperatures ranged 300–800 K. The typical T_A^* rms noise achieved was ∼ 0.06 K for a velocity resolution of 0.35 km s^{-1}.

3. Results

3.1. HCO^+ J=4→3

The HCO^+ J=4→3 maps obtained with the raster technique (see Fig. 1) clearly show three clumps of emission. The easternmost and strongest clump coincides with the ammonia core detected by Gómez et al. (1994) and surrounds the YSO that is powering the molecular outflow (Ward-Thompson et al. 1995). The size of the emission (measured from the contour at half-intensity of the integrated emission from Fig. 1) is 26″ × 17″, which corresponds to a deconvolved size of 22″ × 10″ (assuming a Gaussian distribution with uniform density and temperature). This is in agreement with the size of the ammonia and dust emission from the core (Gómez et al. 1994; Ward-Thompson et al. 1995). The J=4→3 line central velocity and width (see Table 1) are also in agreement with those of the NH_3 (1, 1) transition.

The other two clumps (from west to east, JMG99 G1 and G2, see Fig. 1) are located about 95″ and 60″ west of the core, respectively, and lie, in projection, within the blue lobe of the molecular outflow. They have no known YSO associated with them (e. g., from IR images, Margulis et al. 1990). In addition, these two clumps appear coincident or very close to near-IR H_2 knots (Davis & Eislöffel 1995). The line central velocity and width are similar to those of the core (see Table 2), which implies a quiescent nature for the clumps, despite their association with the shock-excited H_2 emission. Quiescent clumps associated with shock-excited H_2 emission have been observed in several outflow shocked regions (see § 5.2).

[10]The Caltech Submillimeter Observatory is funded by the National Science Foundation under contract AST-9615025

We also observed the HCO^+ J=4→3 transition toward selected positions in the red lobe, where near-IR H_2 emission is detected. However, none of the positions showed emission brighter than $T_{\rm MB} \sim 0.4$ K. Table 3 gives the positions and upper limits of these observations.

3.2. HCO^+ J=3→2

The spectra obtained for the HCO^+ J=3→2 line in the core and JMG99 G1 and G2 clumps are shown in Fig. 2. The line parameters for the core and the clumps are shown in Tables 1 and 2. In clump G1 the J=3→2 line has a double peak (note that the J=4→3 spectrum also has a double peak: see Fig 1). One peak is at $v_{\rm LSR} = 5.0 \pm 0.2$ km s^{-1}, and the other at $v_{\rm LSR} = 2.6 \pm 0.2$ km s^{-1}. The higher velocity component has a similar $v_{\rm LSR}$ as those of the core and clump G2.

3.3. HCO^+ J=1→0

HCO^+ J=1→0 line emission was not detected in our OVRO natural weighted maps at a 4-σ level of 0.32 Jy beam^{-1}, with a 0.4 km s^{-1} channel width, or 1.9 K for an angular resolution of $5''$ (§ 2.4). The integrated emission in the $v_{\rm LSR}$ interval from 3 to 6 km s^{-1} was not detected at a 4-σ level of 0.53 Jy beam^{-1} km s^{-1} or 3.2 K km s^{-1}. In order to be more sensitive to extended emission, we applied different Gaussian taper to the visibility data, without detecting the line emission.

The FCRAO HCO^+ J=1→0 observations also showed no emission toward the core and the G1 and G2 clumps down to a level of $T_{\rm MB} \sim 0.38$ K (4-σ level) for a velocity resolution of ~ 0.5 km s^{-1}. However, the averaged spectrum over a region of $\sim 9' \times 5'$ encompassing the core and the clumps G1 and G2 did show broad, weak J=1→0 emission (see Fig. 3), with a line width of ~ 10 km s^{-1}. The spectrum has two intensity peaks at central velocities of $v_{\rm LSR} \simeq 5$ and 10 km s^{-1}. This emission must come from a roughly uniform and extended gas, since we did not detect any emission from the individual spectra within the averaged region. The upper limit from OVRO is consistent with this result. We did detect strong J=1→0 emission $\sim 4'$ west of the core. This emission has a central velocity of $v_{\rm LSR} = 11.5 \pm 0.1$ km s^{-1} and a line width of 1.6 ± 0.2 km s^{-1}. The size of this emitting region is $\sim 4' \times 2'$ (although we have not fully mapped this cloud). The central line velocity and the distance to the core suggest that this emission may not be directly associated with NGC 2264G, although it is likely part of the NGC 2264 giant molecular complex. Inspection of the spectrum averaged over the core shows that this western cloud component at ~ 11 km s^{-1} is a significant contaminant at the 0.2 K level.

Figure 4 shows the J=1→0 spectra observed with the Haystack telescope toward the core, clump G2 and two other positions. The four spectra show weak, broad emission (~ 10 km s^{-1}), similar to the averaged spectrum from the FCRAO observations. This supports the extended nature of the emitting gas.

3.4. Continuum Emission

With OVRO we did not detect continuum emission at 88 GHz down to ~ 8 mJy beam^{-1} (4-σ level). From the spectral energy distribution of the dust continuum derived by Ward-Thompson et al. (1995), the total dust continuum flux density expected at 88 GHz should be between 3 and 10 mJy, which may be consistent with our upper limit.

4. Analysis

Since we have multi-transition observations of the HCO^+ emission, we carried out radiative transfer calculations using the large velocity gradient (LVG) model approximation (e. g., Scoville & Solomon 1974; Goldreich & Kwan 1974) and the microturbulent model approximation (e. g., Leung & Liszt 1976). Our main goal was to use the observed line temperature intensities of the HCO^+ J=4→3, J=3→2, and $H^{13}CO^+$ J=4→3 transitions in order to derive the expected J=1→0 line temperature and compare it with the "anomalous" observed values ("anomalous" because the J=1→0 is much weaker and broader than that from the higher rotational transitions). These models can also be used to constrain the physical properties (kinetic temperature, HCO^+ column density, and H_2 volume density) of the core. We adopt a $^{12}C/^{13}C$ isotropic ratio of 60 (Langer & Penzias 1990).

4.1. LVG Analysis

For the LVG analysis, we use the observed line temperature ratios, $T_{4,3}/T_{3,2}$ and $T^{13}_{4,3}/T_{4,3}$, and $T_{4,3}$ to derive the expected J=1→0 line temperature. We assume that the different transitions and isotopes have the same emitting size. Thus, the deconvolved size obtained from the HCO^+ J=4→3 map is adopted as the emitting size of all the lines (note that if the emission arises from a region with a power-law density and temperature distributions, the deconvolved size could be somewhat larger than the emitting size). In Table 1 we show the line parameters for the different HCO^+ transitions observed toward the core. For the $T^{13}_{4,3}/T_{4,3}$ ratio, both lines were observed with the same telescope (JCMT), with the same angular resolution ($13''.5$). Thus, the antenna temperature ratio gives us directly the radiation temperature ratio, i. e., independent of the beam efficiency and beam coupling factor. From Table 1 we obtain $T^{13}_{4,3}/T_{4,3} = 0.086 \pm 0.024$. The J=3→2 line however was observed with a different telescope (CSO) and a different angular resolution ($26''$). The observed size and the deconvolved size of the core, measured from the J=4→3 map, are $26'' \times 17''$ and $22'' \times 10''$ respectively. Therefore, the line intensity for the J=3→2 transition, if observed with an angular resolution of $13''.5$ will be $\sim (22 \times 10 + 26^2)/(26 \times 17) = 2.0$ times the intensity measured with the CSO. After applying this correction, the $T_{4,3}/T_{3,2}$ ratio is 0.68 ± 0.04. The J=4→3 line intensity, $T_{4,3}$, can be used as a lower limit of the radiation temperature $T_{R\,4,3}$ in order to further constrain the LVG solutions, since $T_{R\,4,3} = T_{4,3}/f$, where f is the beam coupling factor.

Within 1-σ intervals of the observed line ratios, and for $T_{R\,4,3} \gtrsim T_{4,3}$, the LVG solutions are those with a $T_{1,0}/T_{4,3}$ ratio of 1.8–2.3 and a kinetic temperature of $T_{\rm k} \simeq$10–16 K. However, the set of LVG solutions do not constrain very tightly the physical properties of the core. In Fig. 5 we show a set of the LVG solutions in the $n(H_2)$ – $T_{\rm k}$ plane for N(HCO^+)= 3×10^{14} cm^{-3} (note that for different values of N(HCO^+) the set of possible values of $n(H_2)$ and $T_{\rm k}$ changes). From NH_3 observations, Gómez et al. (1994) derived a rotational temperature of $T_{\rm rot}$ = 15 K, which is a good indicator of the kinetic temperature. Since the observed parameters of the HCO^+ J=4→3 emission (size, line central velocity and line width) are similar to those of the NH_3 emission, we assume that the kinetic temperature of the gas where the HCO^+ arises is $\sim$ 15 K. This further restriction does not change the range of $T_{1,0}/T_{4,3}$ solutions, but it better constrains the H_2 volume density and column density of the HCO^+ emission (see Table 4). We note that in the range obtained for $n(H_2)$, the J=1→0 transition should be fully thermalized, while the other transitions observed, J=3→2 and J=4→3, of HCO^+ are subthermally excited.

In Table 2 we show the line parameters for the HCO^+ spectra toward the clumps G1 and G2. We applied the LVG model to clump G2 in order to check if the HCO^+ J=1→0 emission is also "anomalous", and thus elucidate if this "anomaly" is or not local to the core. From the J=4→3 map, the observed and deconvolved diameters of clump G2 are $20''$ and $15''$, respectively. Therefore, the expected J=3→2 line intensity at an angular resolution of $13''\!.5$ will be $\sim (1.27 \pm 0.09) \times (15^2 + 26^2)/20^2 = 2.86 \pm 0.20$, implying a ratio $T_{4,3}/T_{3,2} \simeq 0.30 \pm 0.05$. The LVG solutions for $T_{\rm k} \gtrsim 10$ K, the observed $T_{4,3}$ and the estimated $T_{4,3}/T_{3,2}$ ratio, imply a $T_{1,0}/T_{4,3}$ ratio of 2.4–11 and $T_{\rm k} \simeq$10–35 K. However, the H_2 volume density and the column density of the HCO^+ are not well constrained (see Table 4).

4.1.1. Observed HCO^+ J=1→0 versus LVG analysis

The $T_{1,0}/T_{4,3}$ range derived for the core, 1.8 to 2.3, implies a J=1→0 intensity, if observed with a $13''\!.5$ angular resolution, of $T_{1,0}$ =6.7–8.6 K. Since the deconvolved size for the core emission is $22'' \times 10''$, the line intensity for an angular resolution of (θ/arcsec), will be given by $[(26 \times 17)/(22 \times 10 + \theta^2)] \times (6.7\text{–}8.6)$ K. Thus, for the FCRAO and Haystack angular resolutions, $54''$ and $26''$, the J=1→0 intensities should be 0.9–1.2 K and 3.3–4.2 K, respectively. The upper limit obtained with FCRAO and the value observed with Haystack (see Table 1) are clearly below the predicted LVG values (see Fig. 6).

We do not detect the HCO^+ (J=1→0) line with OVRO down to a 4-σ level of 0.31 Jy beam^{-1} or 1.9 K (see Table 1 and § 3.3). However, as interferometers are insensitive to large scale structures due to the lack of short baselines in the (u, v) plane, we estimate explicitly the magnitude of this effect. The half-power (u, v) radius of the core emission, r, is:

$$\left(\frac{r}{\mathrm{k}\lambda}\right) = 91.02 \left(\frac{\theta_{\rm FWHM}}{\rm arcsec}\right)^{-1} \tag{1}$$

The full width at half-maximum of the HCO^+ emission can be obtained from the deconvolved size: $\theta_{\rm FWHM} \simeq \sqrt{22'' \times 10''} = 15''$, and hence $r \simeq 6$ kλ (or $\sim$ 65 ns at 89.2 GHz). The flux density of a source of intensity $T_{\rm mb}$, observed at a frequency ν, with an observed source diameter θ_S, is:

$$\left(\frac{S_\nu}{\rm Jy}\right) = 8.24 \times 10^{-7} \left(\frac{\theta_S}{\rm arcsec}\right)^2 \left(\frac{\nu}{\rm GHz}\right)^2 \left(\frac{T_{\rm mb}}{\rm K}\right). \tag{2}$$

Since $\theta_S \simeq \sqrt{26 \times 17} = 21''$ (§ 3.1) and $T_{1,0}$ = 6.7–8.6 K (from the LVG analysis), the expected total flux density of the HCO^+ (J=1→0) emission is S_ν =19–25 Jy. The expected and measured fluxes are plotted in Figure 7. Note that OVRO samples (u, v) spacings down to 3 kλ. The expected correlated flux for (u, v) radii less than $\sim$ 10 kλ is significantly higher than the upper limits of the correlated flux obtained at OVRO, as can be clearly seen in Figure 7.

The LVG analysis in the clump G2 gives a $T_{1,0}/T_{4,3}$ ratio of 2.4–11. Thus, $T_{1,0} \simeq$ 2.1–9.5 K for an angular resolution of $13''\!.5$. Following the same arguments as before, the expected J=1→0 line intensity with the FCRAO and Haystack telescopes should be $\sim$ 0.27–1.2 K and 0.9–4.2 K, which should be detected with Haystack, and possibly marginally detected with FCRAO. In addition, the observed size of $20''$ implies a half-power (u, v) radius for the clump of $\sim$ 6 kλ and a total flux of 5.5–25 Jy, which should also be marginally detected with OVRO with its shortest baselines (see Fig. 7).

Thus, the FCRAO, Haystack, and OVRO observational results compared with the expected line intensity from the LVG analysis suggest that the HCO^+ J=1→0 emission is anomalously weak, especially toward the core.

4.1.2. Mass of the core

The derived H_2 volume density (see Table 4) can be used to roughly estimate the mass of the NGC 2264G core without any assumption on the HCO^+ abundance. Assuming that the geometrical volume of the source is that of a sphere with a diameter equal to the geometrical mean of the major and minor deconvolved axes of the source, 15″ or 0.06 pc, and a helium to hydrogen mass ratio of 30%, we obtain a mass of 0.4–6 $M_\odot$. Alternatively, the mass can also be estimated from the HCO^+ column density derived from the LVG analysis. The HCO^+ relative abundance in molecular clouds ranges from $2\times10^{-10} - 2\times10^{-8}$ (e. g., Irvine, Goldsmith & Hjalmarson 1987; Hasegawa & Mitchell 1995; Blake et al. 1995; Bergin et al. 1997), so we use $X[HCO^+] = 2\times10^{-9}$. For $N(HCO^+) = 3\times10^{14}$–$6\times10^{15}$ cm^{-2} (§ 4.1) and the afore mentioned diameter we obtain a mass of 8–160 $\times$ $(2\times10^{-9}/X[HCO^+])$ $M_\odot$. Previous studies from ammonia and dust observations derived a mass for the core of 6 $M_\odot$ (Gómez et al. 1994) and 2–4 $M_\odot$ (Ward-Thompson et al. 1995). The LVG solution that gives a value for the mass similar to these values, for the two methods used, are those with $n(H_2) \sim 1\times10^6$ cm^{-3} and $N(HCO^+) = 3\times10^{14}$ cm^{-2}. Gómez et al. (1994) derived a H_2 column density from NH_3 observations of $N(H_2) = 1\times10^{23}$ cm^{-2}. Therefore, the fractional abundance of the HCO^+ is $X(HCO^+) \simeq 3\times10^{-9}$, which is in agreement with the values found in the literature.

The LVG solutions for clump G2 do not strongly constrain the HCO^+ column density and H_2 volume density. A rough method to estimate the mass is to assume the same excitation temperature for all the rotational levels, derived from the J=4→3 to J=3→2 line ratio, and to assume optically thin emission. However, since the J=4→3 is likely not thermalized, the population in the lower rotational levels will be underestimated. The total column density derived from the J=4→3 will thus be a lower limit on the true value. From the J=4→3 to J=3→2 line ratio the "averaged" excitation temperature between these two transition is $\sim 9\pm1$ K (e. g., from Eq. 1 and 2 of Girart et al. 1999). From this excitation temperature we derive a beam–averaged column density of $N(HCO^+) = 5\times10^{12}$ cm^{-2}, and from the FWHM size of the J=4→3 emission the mass of the clump G2 is $\sim 0.2\times(3\times10^{-9}/X[HCO^+])$ $M_\odot$.

4.2. Microturbulent Analysis

As an alternative to the LVG model, the data can also be analyzed by using the microturbulent model. The density and temperature are treated in this model as a radial power-law, $(r/r_i)^{-\alpha}$ (see Zhou et al. 1991 for details about the code used). An inner radius, r_i, of 1000 AU (1.″25) was adopted (note that the inner radius is significantly lower than the angular resolution of the different observations). For the temperature, a shallow dependence was assumed, $\alpha = 0.4$ (e. g., Mezger, Smith & Churchwell 1974; van der Tak et al. 1999). The free parameters in the model are the outer radius, r_o, the temperature, T_i, and the density, n_i at the inner radius, the slope of the density power-law, α, and the fractional abundance of the HCO^+. The modeled line intensities were convolved with Gaussians in order to simulate the angular resolutions of the observations. The predicted and observed J=4→3 peak intensities were annularly averaged in order to compare their radial distribution. In addition, to compare the microturbulent model with the OVRO data, we generated visibilities from the modeled HCO^+ J=1→0 line intensity at the same (u, v) points as were sampled by the OVRO interferometer. To check the quality of the model fit we used the reduced χ^2 test as described by Zhou et al. (1991). We ran a number of models for the following range of values of the afore mentioned parameters: $r_o = 1.0\times10^{17}$ – 2.0×10^{17} cm, $T_i = 20$ – 200 K, $n_i = 10^5$ – 10^7 cm^{-3}, $\alpha = 1.0$ – 2.0, $X(HCO^+) = 10^{-10}$ – 10^{-8}.

We found that the observed peak intensities of the HCO^+ J=4→3, J=3→2 and the $H^{13}CO^+$ J=4→3 lines, and the radial intensity distribution of the HCO^+ J=4→3 line do not constrain a unique solution for the afore mentioned parameters, but that there are a number of solutions that fit the data reasonably well. The first consequence of using a model with density and temperature power-law distributions is that the intensity distribution of the raw modeled maps (i.e., before a Gaussian convolution is applied) significantly differ between the different transitions and isotopes. However, once the raw modeled map is convolved with a Gaussian with a similar FWHM as that of the raw intensity distribution, the resulting convolved intensity distribution becomes, in a first approximation, Gaussian: thus, for a line observed with a beam of θ_1, the expected intensity at an angular resolution of θ_2 can be reasonable approximated as $T_1 \times (\theta_1^2 + \theta_{\rm DS}^2)/(\theta_2^2 + \theta_{\rm DS}^2)$, where $\theta_{\rm DS}$ and T_1 are the deconvolved size and intensity measured with the θ_1 beam.

The solutions from the microturbulent analysis do allow us to constrain the physical properties of the core, although not very tightly. We found that the solutions give masses for the core higher than the values previously measured in the literature (see § 4.1.2). Table 5 shows the range of solutions which gives masses of $\lesssim 30 M_\odot$. The excess of mass estimated from the microturbulent analysis may indicate that the core is non-spherical or somewhat clumpy (Zhou et al. 1994: note that J=4→3 map of Fig.1 already suggests departure from spherical geometry. Figure 8 shows the observed and expected radial distribution of the HCO^+ J=4→3 line intensity for the case of $n_i = 3.6 \times 10^6$ cm^{-3}, T_i = 110 K, $\alpha = -1.4$ and $X(HCO^+) \sim 1 \times 10^{-9}$, which gives a core mass of $\sim 12\ M_\odot$.

4.2.1. Observed HCO^+ J=1→0 versus microturbulent analysis

Although the microturbulent analysis does not strongly constrain the physical properties of the core, these models, like those from the LVG analysis, do constrain the possible values of the HCO^+ J=1→0 intensity. We found that for a 13.″5 angular resolution, $T_{1,0}/T_{4,3}$ ranges roughly from 3 to 5, which is higher than the ratio derived from the LVG analysis (note that this result does not change even if we take into account all the possible microturbulent solutions, independent of the mass derived). For the specific parameters of the solution shown in Fig. 8, the expected HCO^+ J=1→0 line intensities for a beam of 26″ and 54″ are 7.6 K and 2.3 K, which should have been easily detected by these two telescopes. In addition, the expected correlated flux should have also been easily detected by OVRO (see Fig. 7).

5. Discussion

5.1. The Cold Low-Density Envelope

5.1.1. Absorption of the HCO^+ J=1→0 Emission

From the LVG and microturbulent analysis carried out in the previous section, the HCO^+ J=1→0 emission from the core and the clump G2 should have been clearly detected with the FCRAO, Haystack and OVRO instruments. A maser pump mechanism could explain the anomalous population among the various energy levels, but masers have tiny sizes when compared with the typical size of a dense core. A more likely explanation for the anomalous low intensity of the HCO^+ J=1→0 emission is that a cold low-density molecular cloud lies in the foreground, perhaps as part of an envelope surrounding the NGC 2264G region. This low density material could absorb the radiation coming from the high-density gas of the core and the clumps. A somewhat similar situation was found in L134N by Langer et al. (1978). In this region, the $H^{13}CO^+$ J=1→0 is stronger that the HCO^+ J=1→0 at the velocity of the $H^{13}CO^+$ peak intensity, whereas the HCO^+ is very asymmetrical and peaks at a different velocity than the $H^{13}CO^+$ (Langer et al. 1978)).

Lada & Fich (1996) suggest that in NGC 2264G, the CO emission in the 4–12 km s^{-1} $v_{\rm LSR}$ range is contaminated by emission from various clouds associated with the NGC 2264 giant cloud complex, which overlap along the line of sight. One of the primary components of these clouds lies in the 4–6 km s^{-1} $v_{\rm LSR}$ range, i.e., at the same velocities as the HCO^+ J=3→2 and J=4→3 emission from the core and the clumps G1 and G2. This CO component extends over a region larger than the extent of the molecular outflow. The HCO^+ J=1→0 spectrum from Haystack (see Fig. 4) does not show clearly the different velocity components as seen in the CO emission, but extends roughly over the same velocity range as the CO. In addition, the J=1→0 FCRAO spectrum averaged over a region encompassing the core and the clumps G1 and G2 (see § 3.3 and Fig. 3) shows two main components, one at $\sim$ 5 km s^{-1} and the other at $\sim$ 10 km s^{-1}, which coincide with two of the CO components. Therefore, we conclude that the HCO^+ J=1→0 emission detected with Haystack and FCRAO may arise from the ambient gas in several extended clouds, as does the CO emission in the lower J transitions over the same velocity range.

The cold low-density cloud associated with the component at $\sim$ 5 km s^{-1} may efficiently absorb the J=1→0 emission from the core if this cloud is located in the foreground of NGC 2264G. This foreground cloud can be characterized by its excitation temperature, $T_{\rm fg}$, and its optical depth, $\tau_{\rm fg}$. The radiative transfer equation for the emission of the HCO^+ J=1→0 at $v_{\rm LSR} \simeq 5$ km s^{-1} can be expressed as

$$T_{\rm obs} = T_{\rm c}\, e^{-\tau_{\rm fg}} + \left(J(T_{\rm fg}) - J(T_{\rm bg})\right)\,\left(1 - e^{-\tau_{\rm fg}}\right) \qquad (3)$$

where $T_{\rm c}$ is the main-brightness temperature of the core, estimated from the LVG model calculations (see § 4.1.1). For the Haystack observations of the core we have $T_{\rm obs} \simeq 0.4$ K. From the LVG analysis we found that $T_{\rm c} \simeq 3.3$ K for a telescope with the Haystack angular resolution (see § 4.1.1). Using these values, the above equation can be written as

$$J(T_{\rm fg}) = \frac{1.5 - 4.4\, e^{-\tau_{\rm fg}}}{1 - e^{-\tau_{\rm fg}}}. \qquad (4)$$

This equation has physically plausible solutions for values of $T_{\rm fg}$ between 2.8 and 3.2 K, and $\tau_{\rm fg}$ larger than 2.2. This range of excitation temperatures is significantly below the value of the kinetic temperature, 10 K, estimated from the CO data of Margulis et al. (1990), and close to the microwave background radiation temperature. This indicates that the volume density of the foreground cloud is significantly lower than the critical density of the HCO^+ J=1→0 transition ($n_{\rm fg} \ll 10^4$ cm^{-3}). This is because for these densities and temperatures the collisional de-excitation rate of the HCO^+ $J = 1$ level is much lower than the rate of spontaneous emission, i.e., the radiative excitation completely dominates over the collisional excitation and, therefore, in the absence of a strong source of radiation, $T_{\rm ex}$ should be close to the background radiation temperature, 2.78 K (Langer et al. 1978). Furthermore, such a low density implies that the higher rotational levels are likely to be almost completely depopulated and, thus, almost transparent to the radiation arising from the core. This is supported by the results of the LVG analysis of the HCO^+ J=4→3 and J=3→2 emission, which give a mass in agreement with previous results, indicating that the opacity of the foreground cloud is not affecting significantly these two transitions. Thus, we assume an J=3→2 optical depth for the foreground cloud no greater than 0.3 (i.e., the foreground cloud is absorbing less than $\sim$ 25% of the J=3→2 radiation from the core), which allows us to better constrain the optical depth of the foreground HCO^+ J=1→0 transition. Since $T_{\rm fg} \simeq T_{\rm bg}$, all the rotational levels of the HCO^+ in the foreground cloud should have nearly the same excitation temperature. When all the rotational levels have the same excitation temperature, the total column density for a linear, rigid rotor molecule is given by (e.g., Garden et al. 1991):

$$N = \frac{3k}{8\pi^3 B\mu^2 J}\frac{T_{\rm ex} + hB/3k}{1 - e^{-2hBJ/kT_{\rm ex}}}\Delta v\, \tau_{J,J-1}\, e^{hBJ(J-1)/kT_{\rm ex}} \qquad (5)$$

where B is the rotational constant, and μ is the permanent dipole moment of the molecule. From this equation the ratio of opacities for two HCO^+ transitions is given by:

$$\frac{\tau_{J_1,J_1-1}}{\tau_{J_2,J_2-1}} = \frac{J_1}{J_2}\,\frac{e^{4.28\,J_1/T_{\rm ex}}-1}{e^{4.28\,J_2/T_{\rm ex}}-1}\,e^{-(2.14/T_{\rm ex})[J_1(J_1+1)-J_2(J_2+1)]}, \tag{6}$$

Therefore, assuming a J=3→2 optical depth of $\lesssim 0.3$, the possible values for $\tau_{\rm fg}$ ranges from 2.2 to 8. We adopt $\tau_{\rm fg} = 4$ and $T_{\rm fg} \simeq 3.2$ K, and should thus be able to estimate the foreground cloud column density to within a factor of ~ 2. From Eq. 5, the HCO^+ column density of the foreground cloud is given by:

$$\left[\frac{N_{\rm fg}({\rm HCO^+})}{\rm cm^{-2}}\right] = 2.46\times10^{11}\left(\left[\frac{T_{\rm fg}}{\rm K}\right]+0.71\right)\left[\frac{\Delta v}{\rm km\,s^{-1}}\right]\tau_{\rm fg}\left(1-e^{-4.28\,/\,[T_{\rm fg}/{\rm K}]}\right)^{-1}. \tag{7}$$

Thus, for $\Delta v = 1.3$ km s^{-1} (see Table 1) and the values given above, the column density is $N_{\rm fg}({\rm HCO^+}) \simeq 6.7\times10^{12}\,{\rm cm^{-2}}$. Assuming an HCO^+ relative abundance of 3×10^{-9} (see § 4.1.2) the foreground cloud that is absorbing the J=1→0 emission from the core has a H_2 column density of $N_{\rm fg}({\rm H_2}) \simeq 2.3\times10^{21}\,(X[{\rm HCO^+}]/3\times10^{-9})^{-1}\,{\rm cm^{-2}}$. Margulis et al. (1990) found from CO observations that the ambient cloud column density, away from the core position, is $N({\rm H_2})\simeq 2.8\times10^{21}\,{\rm cm^{-2}}$, which is fully consistent with the existence of the foreground cloud.

5.1.2. *Absorption of Other Molecular Lines*

We note that this behavior of a foreground cloud, absorbing efficiently the HCO^+ J=1→0 line, but not the higher rotational transitions, will also occur for the rotational transitions of other abundant high density tracer molecules with similar or higher critical densities. We calculated for different tracers the effect of the foreground cloud on the emission coming from the core. Since the density of the foreground cloud is small, the excitation temperature of other high density tracers for the foreground cloud will also have a low value. Therefore, we assume that the excitation temperature is similar to that of HCO^+ (i.e., $T_{\rm fg} \simeq 3.2$ K). The opacity for a given linear, rigid rotor molecule can be obtained from Eq. 5. In practical units, and for $T_{\rm ex} = 3.2$ K, $\Delta V = 1.3$ km s^{-1}, and $N({\rm H_2}) = 3.4\times10^{21}$ cm^{-2}, the $J\rightarrow J-1$ optical depth is given by:

$$\tau_{J,J-1} = 16\,B_{11}J\left[\frac{\mu}{\rm D}\right]^2\left[\frac{X}{10^{-8}}\right]\frac{\left(1-e^{-3.0B_{11}J}\right)e^{-1.5B_{11}J(J-1)}}{3.2+1.6B_{11}} \tag{8}$$

where X is the fractional abundance of the molecule and B_{11} is the rotational constant of the molecule in units of 100 GHz. In Table 6 we show the expected optical depths of the foreground cloud for different molecules and transitions. It is clear that the effect of the foreground cloud is quite different depending on the molecule and transition. Thus, for example, the core's emission from high density tracers such as CS or NH_3 will only be mildly to slightly affected by the foreground cloud. On the other hand, the foreground cloud is completely opaque to the HCN J=1→0 line emission from the core. In general, the higher rotational transitions used are less affected by the foreground cloud. This is because the volume density of the foreground cloud ($n_{\rm fg} \ll 10^4$ cm^{-3}) is so small that the high density tracers are populated only in their lowest rotational states. The rare isotopes of the molecules are not strongly affected by the foreground cloud, so they should be used to study the core properties if the J=1→0 rotational transition is being used. The ^{13}CO and $C^{18}O$ lines have critical densities small enough to have their emission from the foreground thermalized, i.e., their excitation temperature is likely to be closer to 10 K (the typical temperature of molecular clouds), instead of the 3.2 K derived for the HCO^+. Therefore, to estimate their optical depth from the foreground cloud, we used a excitation temperature of 10 K. For the ^{13}CO line, the foreground cloud is moderately opaque to the core emission for rotational transitions up to $J = 3$, whereas in the $C^{18}O$ line, the foreground cloud is essentially transparent. Further multi-transition observations of different molecules will be needed to unambiguously confirm the presence of the foreground cloud and to better constrain its properties (e. g., column density and volume density). We note that even though the strong absorption of the lowest rotational transition of the HCO^+ in the core of NGC 2264G can be considered as exceptional, this result may indicate that in other dense cores, especially those within GMCs, there could also be a foreground cold low density cloud, which might affect the core emission of the J=1→0 line of the HCO^+ and other high dipole moment species such as HCN. Thus, the properties derived from observations of just this transition will be affected. In these cases, rare isotopes of these molecules or higher rotational transitions should be used to study the dense cores.

5.2. The Nature of the Clumps JMG99 G1 and G2

The presence of two dense clumps close to strongly shocked regions, as traced by the near-IR H_2 emission, with almost no sign of direct perturbation (i. e., emission characterized by narrow line widths and a $v_{\rm LSR}$ velocity similar to the core) is not an unusual phenomenon. Several Herbig-Haro objects lie close to quiescent clumps, which have been detected mainly by HCO^+ and NH_3 observations (HH 7-11: Rudolph & Welch 1988; HH 1-2: Davis, Dent & Bell Burnell 1990; Torrelles et al. 1992, 1993; HH 34: Rudolph & Welch 1992; HH 80 N: Girart et al. 1994; Girart, Estalella & Ho 1998). In a clumpy model of star-forming cores (e. g., Taylor, Morata & Williams 1996), these quiescent condensations associated with strong interstellar shocks can be understood as transient density enhancements that are exposed to the UV radiation from the shock (Taylor & Williams 1996). This irradiation releases icy mantles from the dust grains and induces a photon dominated chemistry. Subsequently, a number of molecules have their emission enhanced, HCO^+ and NH_3 among them (Taylor & Williams 1996; Viti & Williams 1999, Raga & Williams 2000).

Weak ($T_{\rm mb} \simeq 0.1$ K) blueshifted emission down to velocities of $v_{\rm LSR} \simeq -1$ km s^{-1} is detected in the HCO^+ J=3→2 spectrum toward the clump G2 (see Fig. 2). Note that this component is detected neither in the J=4→3 spectrum (due to its poorer sensitivity) nor in the J=3→2 spectrum toward clump G1 (Fig. 1 and 2). Interestingly, blueshifted CO emission, in the same velocity range of blueshifted HCO^+ emission, is stronger toward clump G1 than toward clump G2, with the peak intensity about $20''$ south of clump G1 (see Fig 4d from Fich & Lada 1998). This kind of "anti-correlation" between the high velocity blueshifted HCO^+ and CO emission and the presence of shock-excited H_2 at the position of clump G2 suggests that the high velocity HCO^+ emission is likely enhanced and tracing shocked gas, as observed for example in the NGC 2071 molecular outflow (Girart et al. 1999). This implies that part of the clump G2 may be affected by the outflow.

6. Conclusions

We have carried out multi-transition observations of the HCO^+ molecule to study the very young star forming region in NGC 2264G. The main results are:

- From the map of the HCO^+ J=4→3 and the HCO^+ J=3→2 spectra taken at selected positions, we detect the dense core encompassing the exciting source of the molecular outflow. The properties of the emission (e. g., size, line width) are in agreement with previous ammonia observations.

- Taking into account the results from previous (ammonia and dust continuum) observations and from the LVG analysis carried out using the HCO^+ J=4→3 and J=3→2 transitions, and $H^{13}CO^+$ J=4→3 spectra we found that the volume density of the dense core, as traced by the HCO^+, is $n(H_2) \simeq 1 \times 10^6$ cm^{-3}. The relative abundance of the HCO^+ is $X(HCO^+) \simeq 3 \times 10^{-9}$.

- Two quiescent clumps, JMG99 G1 and G2, are detected close to shock excited near-IR H_2 knots. These clumps belong to the class of radiatively excited clumps, i. e., the radiation from the shock evaporates the dust mantles and initiates a photochemical processing, enhancing the emission from HCO^+.

- In contrast with the higher rotational transitions, the HCO^+ J=1→0 spectra show an anomalous emission, i. e., its line intensity toward the core (and toward the quiescent clumps) is much weaker, and the line width is much broader than those measured from the J=4→3 and J=3→2 lines. Inspection of HCO^+ J=1→0 spectra at different positions suggests that this emission comes from a region much larger than the core.

- The results of LVG and microturbulent analyses predict an HCO^+ J=1→0 line intensity toward the dense core several times stronger than the actual value measured with several instruments (OVRO, FCRAO and Haystack).

- The anomalous properties of the HCO^+ J=1→0 emission toward NGC 2264G suggest that a cold low-density molecular cloud lies in the foreground, perhaps as part of an envelope surrounding the NGC 2264G region, which efficiently absorbs the HCO^+ J=1→0 radiation arising from the core. Previous CO observations suggest that in the 4–12 km s^{-1} $v_{\rm LSR}$ range (approximately the range at which the HCO^+ J=1→0 is detected) the CO emission is contaminated by emission from various clouds, which supports the foreground cloud hypothesis.

- We estimated the excitation temperature and column density of the foreground cloud and made predictions of its expected optical depths for various molecules and transitions. We found that the core emission from lines such as HCN J=1→0 should be strongly affected by the foreground cloud absorption, whereas the J=1→0, J=2→1 and J=3→2 transitions of CS and ^{13}CO should be only moderately absorbed. Further, the inversion transitions of ammonia, $C^{18}O$ emission, and that from the rare isotopes of the HCN and HCO^+ should be unaffected by the foreground cloud.

- The afore mentioned result may indicate that in other dense cores, especially those within GMCs, there could also be a foreground cold low density cloud, which might affect the core emission of the J=1→0 line for molecules such as HCO^+ or HCN, and thus affect the properties derived from observations of just this transition. In these cases, the rare isotopes of these molecules and higher rotational transitions of the main isotopes should be used to study these regions.

- We detected a dense ambient cloud 4′ west of the NGC 2264G dense core. Its different central velocity, compared with the NGC 2264G core, suggests that this cloud does not belong to the NGC 2264G region, though it is likely part of the NGC 2264 GMC.

We thank Q. Zhang for helping us during the JCMT observations. We thank C. J. Davis for providing us the H_2 image of NGC 2264G. We would like to thank the anonymous referee for the valuable comments. JMG acknowledges partial support from a Smithsonian predoctoral fellowship. JMG is supported by NFS grant AST-9613999. RE acknowledges the fellowship 1999BEAI400053 from the Comissionat per a Universitats i Recerca, and is partially supported by DGICYT grant PB98-0670 (Spain). ALR wishes to acknowledge the support of the NSF Young Faculty Career Development CAREER Program via NSF grant 96-24924. JMG and RE acknowledge the hospitality of the CfA during the preparation of this paper.

REFERENCES

Anglada, G., Estalella, R., Mauersberger, R., Torrelles, J. M., Rodríguez, L. F., Cantó, J., Ho, P. T. P., & D'Alessio, P. 1995, ApJ, 443, 682

Blake, G. A., Sandell, G., van Dishoeck, E. F., Groesbeck, T. D., Mundy, L. G., & Aspin, C. 1995, ApJ, 441, 689

Bergin, E. A., Ungerechts, H., Goldsmith, P. F., Snell, R. L., Irvine, W. M., & Schloerb, F. P. 1997, ApJ, 482, 267

Curiel, S., & Rodríguez, L.F. 1989, Rev.Mexicana Astron. Af., 17, 115

Davis, C. J., Dent, W. R. F., & Bell Burnell, S. J. 1990, MNRAS, 244, 173

Davis, C. J., & Eislöffel, J. 1995, A&A, 300, 851

Fich, M., & Lada, C.J. 1997, ApJ, 484, L63

Fich, M., & Lada, C.J. 1998, ApJS, 117, 147

Garden, R. P., Hayashi, M., Gatley, I., Hasegawa, T., & Kaifu, N. 1991, ApJ, 374, 540

Girart, J. M., Estalella, R., & Ho, P.T.P. 1998, ApJ, 495, L59

Girart, J. M., Ho, P.T.P., Rudolph, A. L., Estalella, R., Wilner, D. J., & Chernin, L. M. 1999, ApJ, 522, 921

Girart, J. M., et al. 1994, ApJ, 435, L145

Goldreich, P., & Kwan, J. 1974, ApJ, 189, 441

Gómez, J.F., Curiel, S., Torrelles, J.M., Rodríguez, L.F., Anglada, G., & Girart, J.M. 1994, ApJ, 436, 749

Hasegawa, T.I., & Mitchell, G.F. 1995, ApJ, 441, 665

Heaton, B. D., Little, L. T., Yamashita, T., Davies, S. R., Cunningham, C. T., & Monteiro, T. S. 1993, A&A, 278, 238

Hogerheijde, M. R., van Dishoeck, E. F., Blake, G. A., & van Langevelde, H. J. 1997, ApJ, 489, 293

Irvine, W.M., Goldsmith, P.F., & Hjalmarson, A. 1987, in Interstellar Processes, ed. D.J. Hollenbach & H. A. Jr. Thronson (Dordretch: Reidel), 561

Lada, C.J., & Fich, M. 1996, ApJ, 459, 638

Langer, W. D., Wilson, R. W., Henry, P. S., & Guélin, M. 1978, ApJ, 225, L139

Langer, W. D., & Penzias, A. A. 1990, ApJ, 357, 477

Leung, C.-M., & Liszt, H. S. 1976, ApJ, 208, L732

Margulis, M. & Lada, C.J. 1986, ApJ, 309, L87

Margulis, M., Lada, C.J., & Snell, R.L. 1988, ApJ, 233, 316

Margulis, M. et al. 1990, ApJ, 352, 615

Mezger, P. G., Smith, L. F., & Churchwell, E. 1974, A&A, 32, 269

Raga, A. C., & Williams, D. A. 2000, submitted to the A&A

Rudolph, A., & Welch, W. J., 1988, ApJ, 326, L31

Rudolph, A., & Welch, W. J., 1992, ApJ, 395, 488

Scoville, N. Z., & Solomon, P. M. 1974, ApJ. 187, L67

Taylor, S. D., Morata, O., & Williams, D. A. 1996, A&A, 313, 269

Taylor, S.D., & Williams, D. A. 1996, MNRAS, 282, 1343

Torrelles, J. M., Rodríguez, L. F., Cantó, J., Anglada, G., Gómez, J. F., Curiel, S., & Ho, P. T. P. 1992, ApJ, 396, L95

Torrelles, J. M., Gómez, J. F., Ho, P. T. P, Anglada, G., Rodríguez, L. F., & Cantó, J. 1993, ApJ, 417, 655

van der Tak, F. F. S., van Dishoeck, E. F., Evans II, N. J., Bakker, E. J., & Blake, G. A. 1999, ApJ, 522, 1010

van Dishoeck, E. F., Blake, G. A., Jansen, D. J., & Groesbeck, T. D. 1995, ApJ, 447, 760

Viti, S., & Williams, D. A. 1999, MNRAS, 310, 517

Ward-Thompson, D., Eiroa, C., & Casali, M.M. 1995, MNRAS, 273, L25

Zhou, S., Butner, H. M., Evans II, N. J., Güsten, R., Kutner, M. L. , & Mundy, L. G. 1994, ApJ, 428, 219

Zhou, S., Evans II, N. J., Güsten, R., Mundy, L. G., & Kutner, M. L. 1991, ApJ, 372, 518

Fig. 1.— Contour map of the integrated HCO^+ J=4→3 emission observed with the JCMT telescope for $3 \leq v_{\rm LSR} \geq 6$ km s^{-1} overlayed with the 2μm H_2 emission (grey scale). Contours are $\pm 2, 3, 4, 5, 6, 8, 10, 12, 14 \times 0.28$ K km s^{-1} (1-σ). In the top panels we show the HCO^+ J=4→3 spectra for the positions of the JMG99 G1 and G2 clumps, and NGC 2264G core, as well the $H^{13}CO^+$ J=4→3 spectrum toward the core. The JCMT beam ($13''.5 \times 13''.5$) is shown in the bottom left corner. The star marks the position of the radio continuum source VLA 2 (Gómez et al. 1994).

Fig. 2.— HCO^+ J=3→2 spectra observed with the CSO telescope at the positions of the clumps JMG99 G1 and G2, and the NGC 2264G core.

Fig. 3.— Contour map of the HCO^+ J=1→0 integrated emission observed with the FCRAO telescope for $3 \leq v_{\rm LSR} \geq 6$ km s^{-1} (lower panel) and 9.0 to 13.5 km s^{-1} (central panel). Contours are separated by 0.33 K km s^{-1} and begin at the level of 0.44 K km s^{-1} (2-σ). The beam is shown in the upper left corner of the lower map. The star shows the position of the VLA 2 source in the NGC 2264G core, and the crosses the positions of the JMG99 G1 and G2 clumps. The top panels show the spectra averaged over the region indicated by the dotted lines. The dashed lines indicate the velocity of the NGC 2264G core.

Fig. 4.— HCO^+ J=1→0 spectra observed with the Haystack telescope at different positions, including the clump JMG99 G2 and the NGC 2264G core.

Fig. 5.— Set of LVG solutions in the $T_{\rm k}$ – $n(H_2)$ plane, for the observed line intensity ratios, assuming an HCO^+ column density of 3×10^{14} cm^{-2}. The solid and dashed lines are the contours for the observed $T_{4,3}/T_{3,2}$ and $T^{13}_{4,3}/T_{4,3}$ ratios. The thick grey line is the contour for $T_{4,3}$ = 3.71 K, i.e., the radiation temperature for this transition if f=1. Solutions with $f < 1$ are those above this line. The dotted lines indicate the range of expected values for the $T_{1,0}/T_{4,3}$ ratio.

Fig. 6.— Observed HCO^+ J=1→0 spectra at the core with Haystack (left) and FCRAO (right) *versus* the lower limit of the expected intensity of this line from the LVG analysis (dotted line).

Fig. 7.— OVRO correlated flux in the (u, v) plane for the observed visibilities (filled circles), the lower limits of the expected flux from the LVG analysis (solid lines) and the expected flux from the microturbulent analysis (dashed lines) from the NGC 2264G core (left panel) and JMG99 G2 clump (right panel). The dotted lines show the expected value for the amplitude assuming no signal (i.e., the "zero bias").

Fig. 8.— Radial profile of the HCO^+ J=4→3 peak line intensity. The filled circles show the JCMT data; the solid line show the best-fit microturbulent model (see Table 5).

Table 1. Line parameters of the observed HCO^+ transitions in the core

Molecule	Transition	Telescope	Beam ($''$)	$T_{\rm MB}$ (K)	$v_{\rm LSR}$ (km s^{-1})	ΔV (km s^{-1})
HCO^+	J=4→3	JCMT	14	3.71 ± 0.16	4.55 ± 0.04	1.06 ± 0.09
$H^{13}CO^+$	J=4→3	JCMT	14	0.32 ± 0.09	4.56 ± 0.15	1.60 ± 0.33
HCO^+	J=3→2	CSO	26	2.72 ± 0.08	4.58 ± 0.01	1.29 ± 0.04
HCO^+	J=1→0	OVRO	5	< 1.9	···	···
HCO^+	J=1→0	Haystack	25	~ 0.4	~ 6.4	~ 11
HCO^+	J=1→0	FCRAO	54	< 0.38	···	···

Table 2. Line parameters of the observed HCO^+ transitions in JMG99 G1 and G2

Transition	Telescope	Beam (″)	$T_{\rm MB}$ (K)	$v_{\rm LSR}$ (km s^{-1})	ΔV (km s^{-1})
JMG99 G1[a]					
J=4→3	JCMT	14	0.81 ± 0.26	4.2 ± 0.3	2.5 ± 0.4
J=3→2	CSO	26	0.47 ± 0.12	3.6 ± 0.1	4.5 ± 0.3
J=1→0	FCRAO	54	$\lesssim 0.4$	···	···
JMG99 G2					
J=4→3	JCMT	14	0.86 ± 0.13	4.5 ± 0.2	1.6 ± 0.4
J=3→2	CSO	26	1.27 ± 0.09	4.78 ± 0.03	1.38 ± 0.05
J=1→0	OVRO	5	< 1.9	···	···
J=1→0	Haystack	25	~ 0.4	~ 6.4	~ 11
J=1→0	FCRAO	54	$\lesssim 0.5$	···	···

[a] A single component Gaussian fit was used, although the spectra suggest two components almost blended, and therefore the fit may not be reliable.

Table 3. JCMT HCO^+ J=4→3 limits toward the red lobe

Position ($''$)	$T_{\rm MB}$ [a] (K)
$(+189'', -14'')$	< 0.40
$(+161'', -7'')$	< 0.40
$(+119'', +14'')$	< 0.44
$(+49'', +7'')$	< 0.43

[a] $4-\sigma$ upper limits estimated using $\Delta v = 0.52$ km s^{-1}.

Table 4. Results from the LVG analysis

Region	T_k (K)	$N(HCO^+)$ (cm^{-2})	$n(H_2)$ (cm^{-3})	$T_{1,0}/T_{4,3}$
Core	15[a]	0.3–6$\times 10^{15}$	0.6–10$\times 10^5$	1.8–2.3
JMG99 G2	10–35	2×10^{12}–10^{16}	$\lesssim 1 \times 10^7$	2.4–11

[a]Derived from ammonia observations by Gómez et al. (1994)

Table 5. Results from the microturbulent model

Core Parameter	Value
r_i	1.5×10^{16} cm[a]
r_o	18–25 $\times 10^{16}$ cm
$T_{\rm k}$ at r_i	80–200 K
$T_{\rm k}$ power law index	0.4[a]
$n(\rm H_2)$ at r_i	2–6 $\times 10^6$ cm^{-3}
$n(\rm H_2)$ power law index	1.1–1.5
$X[\rm HCO^+]$	0.5–2.0 $\times 10^{-9}$
$T_{1,0}/T_{4,3}$[b]	3.6–4.1

[a]Fixed parameter in the model.

[b]Ratio for an angular resolution of 13.″5.

Table 6. Expected opacities of the foreground cloud for different molecular lines

Molecule	Abundance[a]	Transition	τ_{fg}[b]
HCO^+	2×10^{-9}	J=1→0	4.0[c]
		J=2→1	2.8
		J=3→2	0.3[c]
		J=4→3	0.007
$H^{13}CO^+$	3×10^{-11}	J=1→0	0.07
HCN	2×10^{-9}	J=1→0	2.8
		J=2→1	1.9
		J=3→2	0.2
		J=4→3	0.005
$H^{13}CN$	3×10^{-11}	J=1→0	0.05
CS	1×10^{-9}	J=1→0	0.2
		J=2→1	0.3
		J=3→2	0.1
		J=4→3	0.02
		J=5→4	0.001
NH_3	1×10^{-8}	$(J, K) = (1, 1)$	0.1[d]
^{13}CO	5×10^{-7}	J=1→0	0.2
		J=2→1	0.4
		J=3→2	0.3
$C^{18}O$	1×10^{-7}	J=1→0	0.04
		J=2→1	0.08
		J=3→2	0.05

[a]Abundances derived toward IRAS 16293-2422 by van Dishoeck et al. (1995). A $^{12}C/^{13}C$ ratio of 60 was adopted (Langer & Penzias 1990).

[b]Derived using the analysis shown in § 5.1.2 for an excitation temperature of 3.2 K, except for the CO isotopes, for which T_{ex} = 10 K.

[c]Values adopted (see § 5.1.1)

[d]Derived using the standard analysis for this molecule (e. g., Anglada et al. 1995) and assuming T_{ex} = 3.2 K.

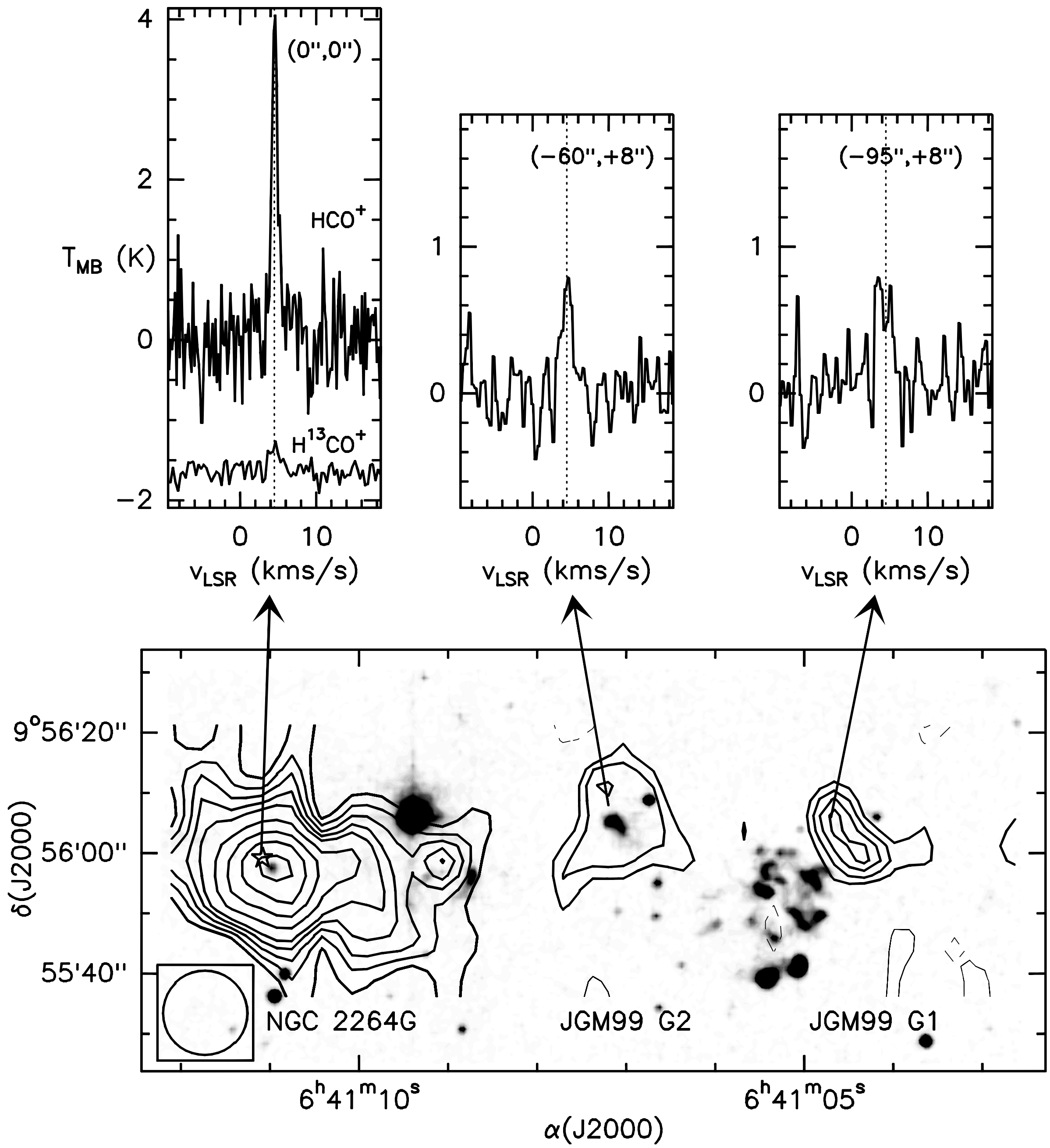
(0'',0'')
HCO+
H13CO+
TMB (K)
(−60'',+8'')
(−95'',+8'')
vLSR (kms/s)
vLSR (kms/s)
vLSR (kms/s)
9°56'20''
56'00''
55'40''
δ(J2000)
NGC 2264G
JGM99 G2
JGM99 G1
6h41m10s
6h41m05s
α(J2000)

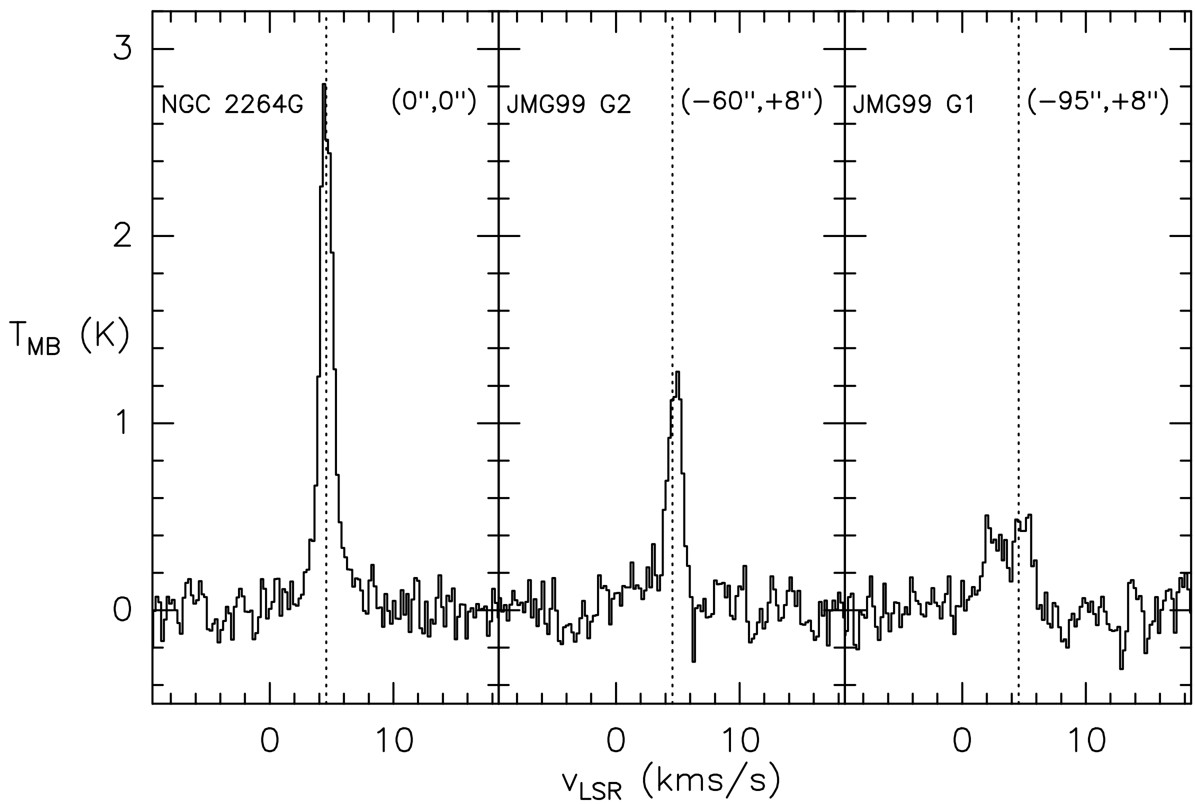

3
2
1
0
T_{MB} (K)
NGC 2264G
(0'',0'')
JMG99 G2
(−60'',+8'')
JMG99 G1
(−95'',+8'')
0
10
0
10
0
10
v_{LSR} (kms/s)

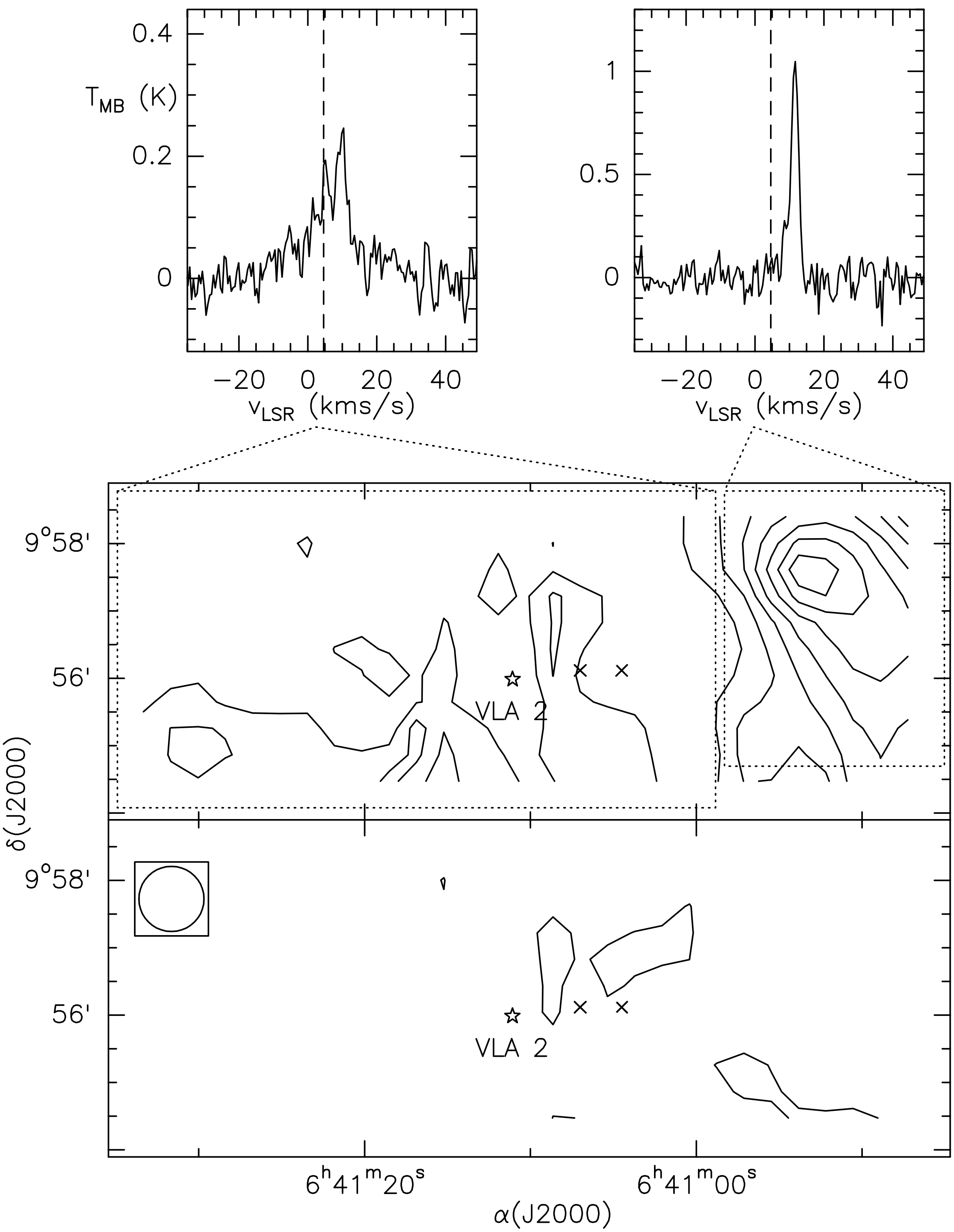

0.4
T_{MB} (K)
0.2
0
−20
0
20
40
v_{LSR} (kms/s)
1
0.5
0
−20
0
20
40
v_{LSR} (kms/s)
9°58'
56'
VLA 2
δ(J2000)
9°58'
56'
VLA 2
$6^h41^m20^s$
$6^h41^m00^s$
α(J2000)

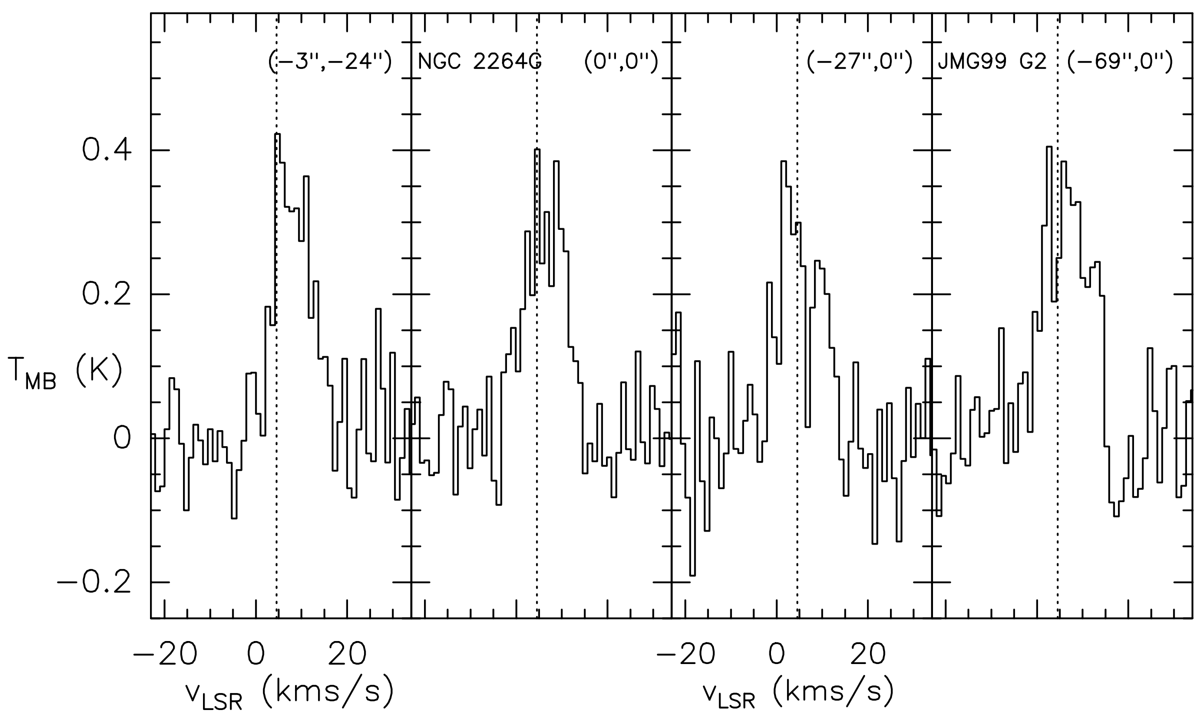
(−3'',−24'')
NGC 2264G
(0'',0'')
(−27'',0'')
JMG99 G2
(−69'',0'')
0.4
0.2
0
−0.2
T_{MB} (K)
−20
0
20
v_{LSR} (kms/s)
−20
0
20
v_{LSR} (kms/s)

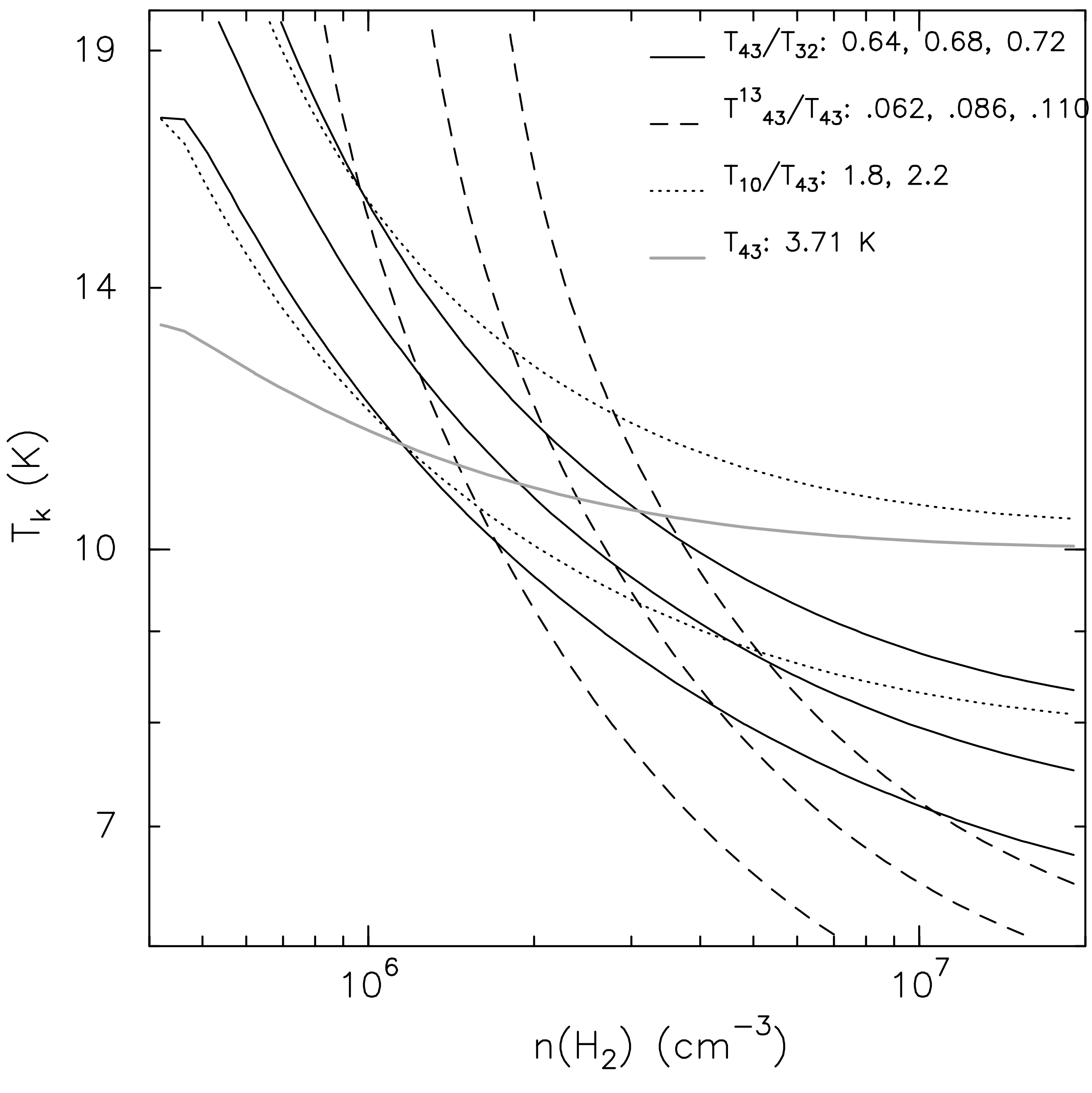
T_{43}/T_{32}: 0.64, 0.68, 0.72
$T^{13}{}_{43}/T_{43}$: .062, .086, .110
T_{10}/T_{43}: 1.8, 2.2
T_{43}: 3.71 K
19
14
10
7
T_k (K)
10^6
10^7
$n(H_2)$ (cm^{-3})

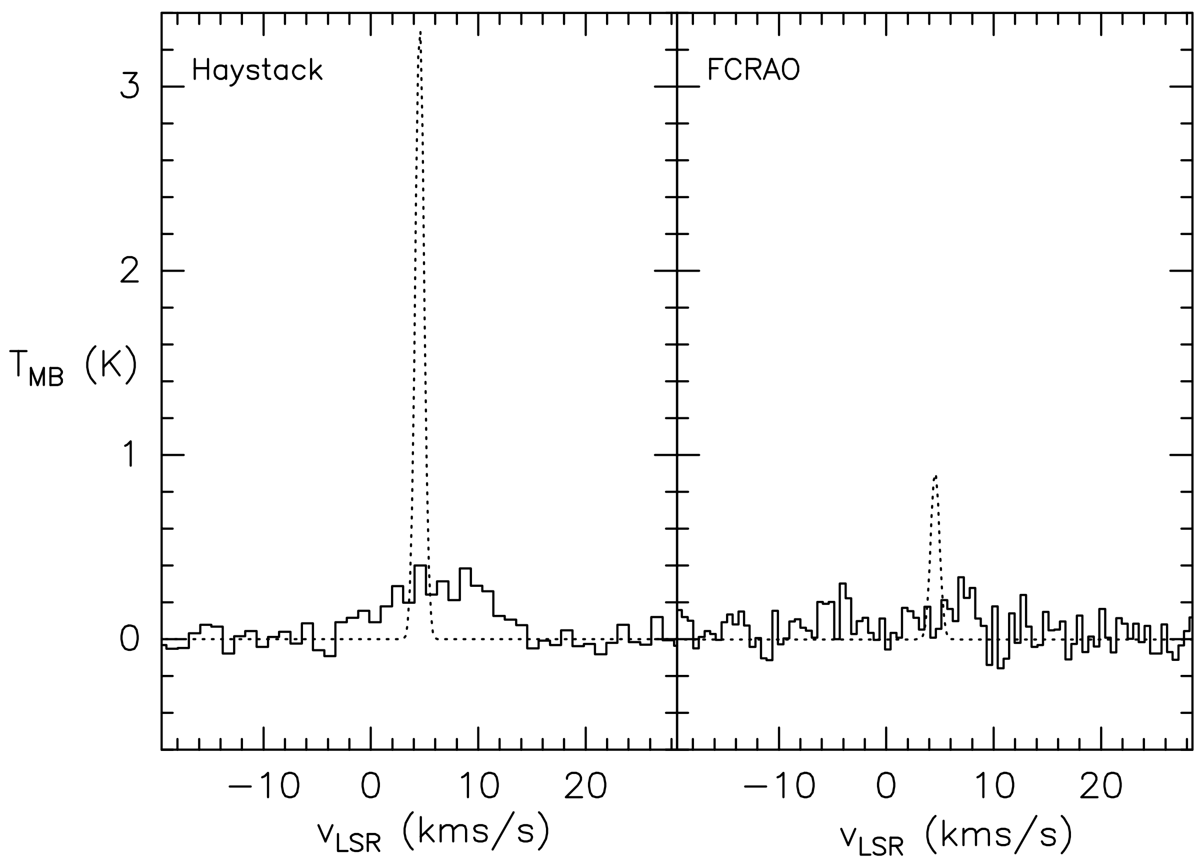
Haystack
FCRAO
3
2
1
0
T_{MB} (K)
−10
0
10
20
v_{LSR} (kms/s)
−10
0
10
20
v_{LSR} (kms/s)

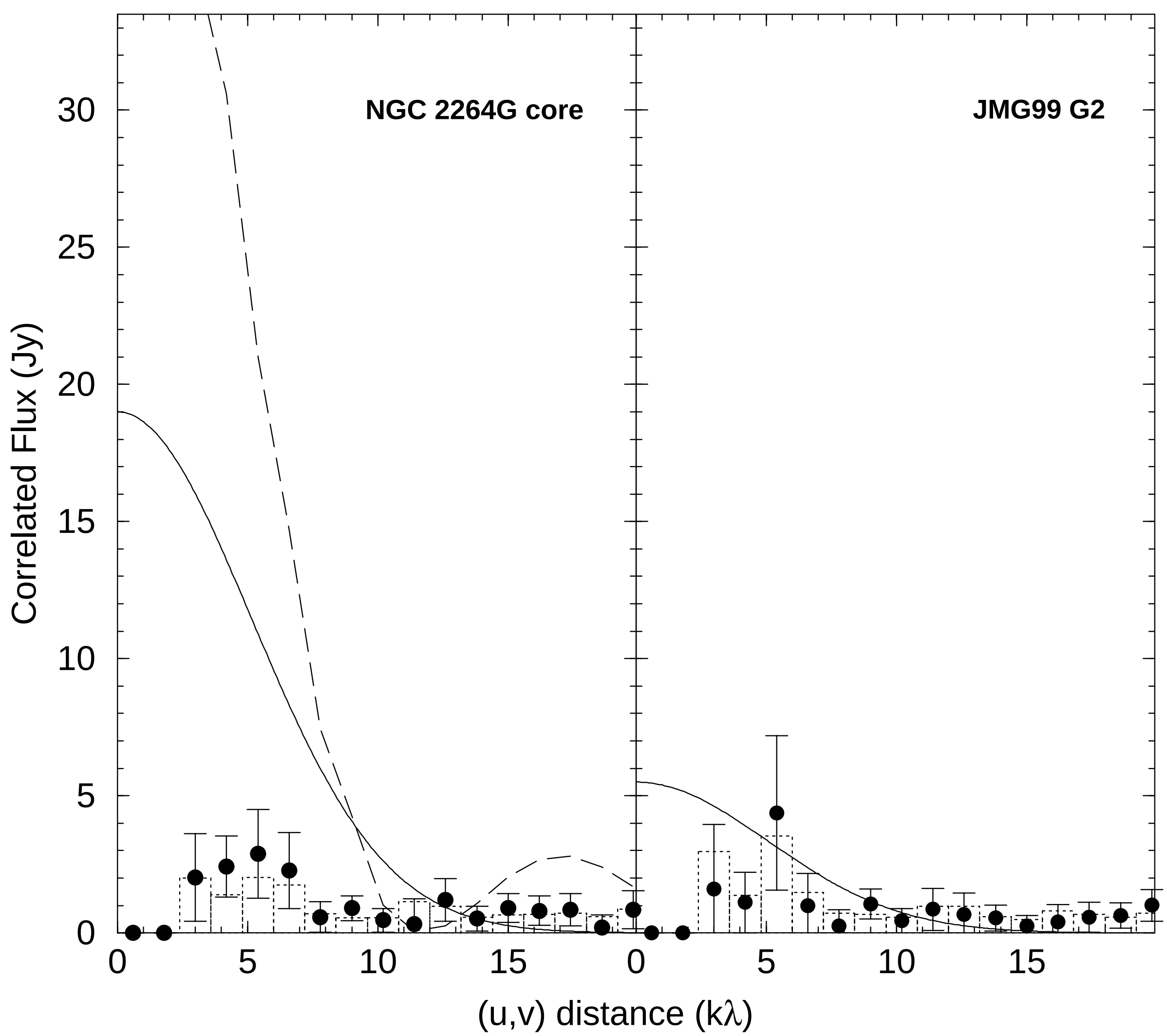
NGC 2264G core
JMG99 G2
Correlated Flux (Jy)
(u,v) distance (kλ)
0
5
10
15
20
25
30

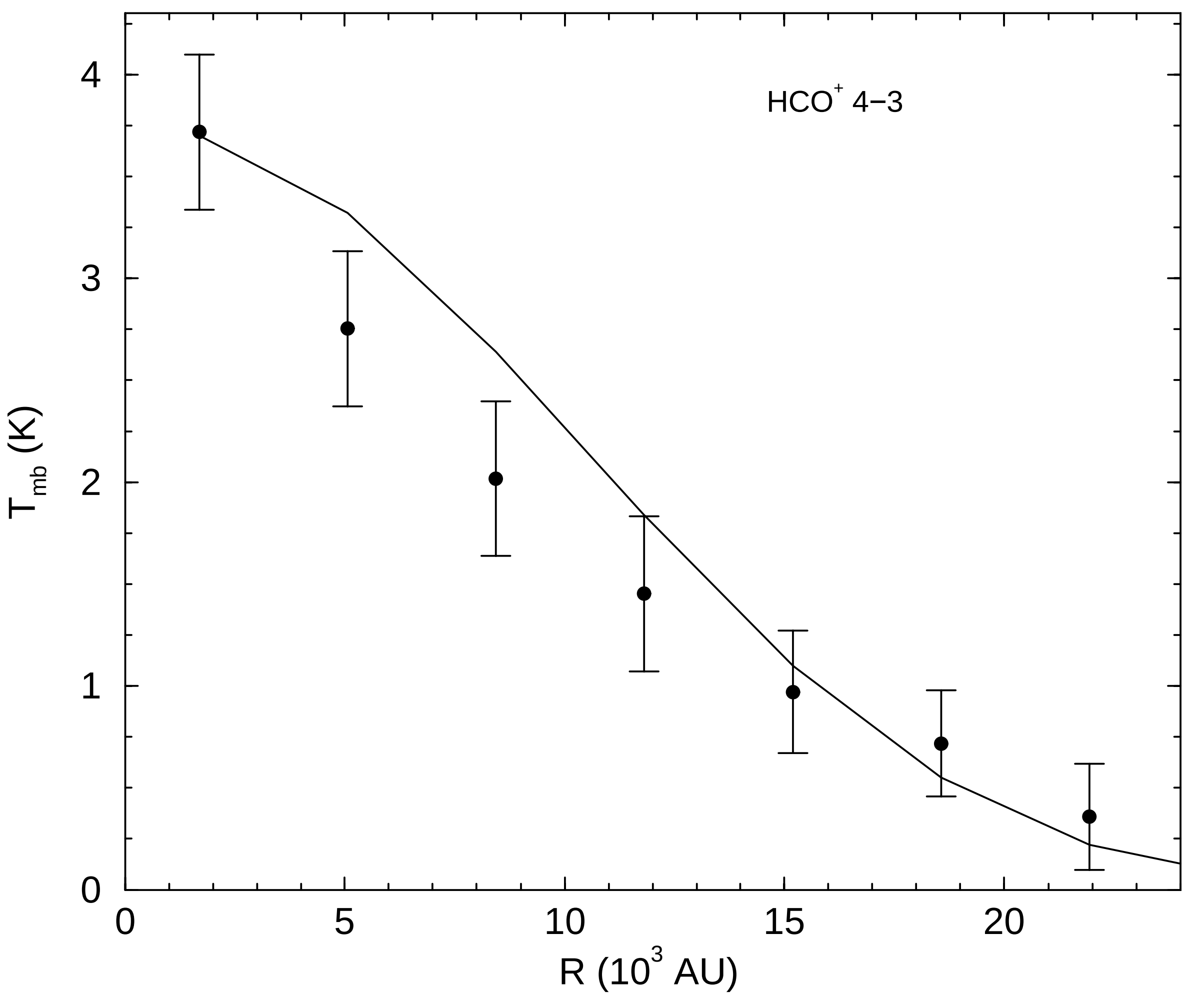
HCO+ 4−3
Tmb (K)
R (10^3 AU)
0
1
2
3
4
0
5
10
15
20